CO Gas Sensing by Ultrathin Tin Oxide Films Grown by Atomic Layer Deposition Using Transmission FTIR Spectroscopy†

X. Du,‡ Y. Du,§ and S. M. George*,‡,§

Departments of Chemical and Biological Engineering and of Chemistry and Biochemistry, University of Colorado, Boulder, Colorado 80309

Received: January 18, 2008; Revised Manuscript Received: June 27, 2008

Ultrathin tin oxide films were deposited on SiO_2 nanoparticles using atomic layer deposition (ALD) techniques with $SnCl_4$ and H_2O_2 as the reactants. These SnO_x films were then exposed to O_2 and CO gas pressure at 300 °C to measure and understand their ability to serve as CO gas sensors. In situ transmission Fourier transform infrared (FTIR) spectroscopy was used to monitor both the charge conduction in the SnO_x films and the gas-phase species. The background infrared absorbance measured the electrical conductivity of the SnO_x films based on Drude−Zener theory. O_2 pressure was observed to decrease the SnO_x film conductivity. Addition of CO pressure then increased the SnO_x film conductivity. Static experiments also monitored the buildup of gas-phase CO_2 reaction products as the CO reacted with oxygen species. These results were consistent with both ionosorption and oxygen-vacancy models for chemiresistant semiconductor gas sensors. Additional experiments demonstrated that O_2 pressure was not necessary for the SnO_x films to detect CO pressure. The background infrared absorbance increased with CO pressure in the absence of O_2 pressure. These results indicate that CO can produce oxygen vacancies on the SnO_x surface that ionize and release electrons that increase the SnO_x film conductivity, as suggested by the oxygen-vacancy model. The time scale of the response of the SnO_x films to O_2 and CO pressure was also measured by using transient experiments. The ultrathin SnO_x ALD films with a thickness of ∼10 Å were able to respond to O_2 within ∼100 s and to CO within ∼10 s. These in situ transmission FTIR spectroscopy help confirm the mechanisms for chemiresistant semiconductor gas sensors.

I. Introduction

Using the electrical conductivity of semiconductor metal oxides for gas detection started with the original work of Seiyama on ZnO[1] and Taguchi[2] on SnO_2 in the 1960s. Semiconductor metal oxide gas sensors are now commercialized and used in a variety of applications.[3,4] These solid-state gas sensors have many advantages such as small size, low cost, simple operation, and chemical stability. However, there are also corresponding disadvantages such as lack of reproducibility, poor selectivity for specific gases, and insufficient sensitivity.[5] Improving the performance of these gas sensors is difficult because the basic mechanism for gas sensing by these semiconductor metal oxides is still under active debate.[6]

The semiconductor metal oxides function as gas sensors because their electrical conductivity is dependent on gas adsorption. There are two main mechanisms proposed for the semiconductor metal oxide gas sensors based on the ionosorption model and oxygen-vacancy model. Both of these models can be used to interpret gas sensor response, and both may be applicable at the same time. According to the ionosorption model,[7−10] O_2 traps conduction electrons on the surface as ionosorbed oxygen species (O_2−, O−, O^{2-}) and reduces the electrical conductivity. Reducing gases, such as CO, then react with oxygen species to form gaseous CO_2 and increase the electrical conductivity by returning the conduction electrons to the metal oxide film. A schematic illustrating the ionosorption model is shown in Figure 1a. The ionosportion model is widely accepted even though spectroscopic investigations have failed to observe the postulated negatively charged oxygen species.[7]

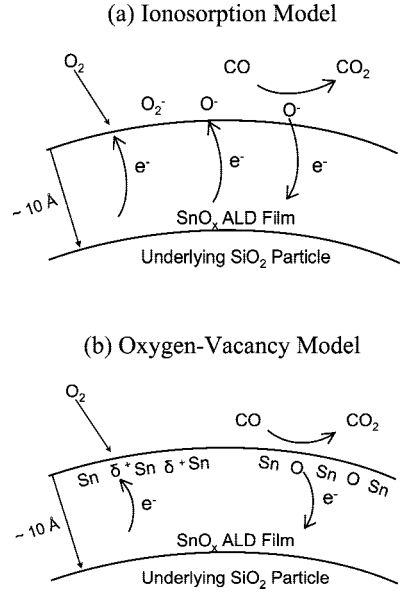

Figure 1. Schematic for O_2 interaction and CO gas sensing by SnO_x film: (a) ionosorption model and (b) oxygen-vacancy model.

The oxygen-vacancy model is also consistent with most observations for semiconductor metal oxide gas sensors.[8,11] In the oxygen-vacancy model, reducing gases, such as CO, react with oxygen in the surface of the metal oxide to produce gaseous

† Part of the "Stephen R. Leone Festschrift".

* Corresponding author. E-Mail: steven.george@coloradu.edu.
‡ Department of Chemical and Biological Engineering.
§ Department of Chemistry and Biochemistry.

10.1021/jp800518v CCC: $40.75
Published on Web 08/16/2008

CO_2. The oxygen vacancy left behind then ionizes and produces an electron in the conduction band of the metal oxide that increases the electrical conductivity. If O_2 is present, the O_2 can refill the oxygen vacancy and recapture the electron from the conduction band and reduce the electrical conductivity. A schematic illustrating the oxygen-vacancy model is displayed in Figure 1b. The oxygen-vacancy model is not discussed as widely as the ionosorption model even though this model predicts the same changes in electrical conductivity.

An important factor affecting the performance of semiconductor metal oxide gas sensors is the grain size or film thickness.[12−15] The grain size or film thickness is important because a space-charge region, that is, a region affected by a loss or gain of charge carriers, is formed under the surface of either the ionosorbed oxygen species in the ionosorption model or the ionized oxygen vacancies in the oxygen-vacancy model. The depth of the space-charge region is correlated with the Debye length and is typically only several nanometers.[12,16,17] Because the electrical conductivity is only changing approximately over the Debye length, the metal oxide grain size or film thickness plays an important role in determining the sensitivity of the metal oxide gas sensor.[18] Many investigations have revealed that the sensitivity of metal oxide gas sensors increases dramatically when using metal oxide nanoparticles,[13−15,19] nanometer thick films,[12] nanowires,[20,21] or nanobelts.[22]

Experiments that can be performed with precise film thicknesses will be able to overcome the variability in sensitivity produced by the finite Debye length. To take advantage of the higher-sensitivity metal oxide films with nanometer thickness, exact nanometer film thicknesses would be desirable for experimental investigations of metal oxide gas sensors. One technique that can produce very accurate and conformal ultrathin film thicknesses is atomic layer deposition (ALD).[23,24] ALD is a gas-phase fabrication process that is based on sequential, self-limiting surface reactions. ALD can be used to deposit many semiconductor metal oxides used as gas sensors such as SnO_2,[25−27] ZnO,[28,29] and TiO_2.[30,31] These semiconductor metal oxides grown by ALD may have many advantages for gas sensors.[32]

In this paper, in situ transmission Fourier transform infrared (FTIR) spectroscopy was utilized to investigate CO gas sensing by ultrathin tin oxide films grown using ALD. CO gas sensing by tin oxide is a model system that has been explored extensively.[14,20−22,33−36] The tin oxide ALD films were deposited on SiO_2 nanoparticles using $SnCl_4$ and H_2O_2 as the reactants. Only 16 $SnCl_4/H_2O_2$ reaction cycles were used to deposit a SnO_x ALD film thickness of ~10 Å that is less than the Debye length for tin oxide.[12] The electrical conductivity of this SnO_x ALD film was then monitored using background infrared absorbance and Drude−Zener theory.[37,38] A series of control experiments were performed to determine the response of this SnO_x ALD film to well-defined O_2, O_2 + CO, and CO gas pressures. The experimental results were then compared with the predictions from the ionosorption and oxygen-vacancy models for semiconductor metal oxide gas sensors.

II. Experimental

The experiments were performed in a viscous-flow ALD reactor specially designed for in situ transmission FTIR studies.[25,39,40] Briefly, the core of the reactor was a four-way cross with 2.75 in Conflat flanges. The entry lines for the reactants and gases were on the front port. Two 1 cm thick CsI salt windows allowed the IR beam to be transmitted through the reactor. Gate valves protected the CsI windows from deposition. A standard six-way cross was connected on the back port. The six-way cross connected to a capacitance manometer for pressure measurements and an Alcatel 2015 mechanical vacuum pump. A sample holder and electrical and thermocouple feedthroughs also connected at the six-way cross. The temperature of the reactor was maintained at 200 °C by a ceramic heater that could be controlled with an accuracy of 0.05 °C.

The substrate was prepared by pressing SiO_2 nanoparticles into tungsten mesh using a stainless-steel die.[29,41,42] The SiO_2 powders were from Aldrich and had an average diameter of 14 nm. The tungsten mesh was from Buckbee Mears Co. and had a spacing of 100 lines/inch and a light transmission of approximately 50%. The substrate had dimensions of 2 cm × 3 cm and a thickness of 50 μm. The SiO_2 nanoparticles had a very high surface area that is necessary for transmission FTIR studies.[29,41,42] In addition to holding the particles, the tungsten grid was used as an electrical heater. A K-type thermocouple was attached on the tungsten mesh. The temperature of the substrate could be controlled accurately using a SIMSPEC 101B temperature controller.

The tin oxide films were deposited on the SiO_2 nanoparticles at 325 °C using ALD techniques. The reactants in the tin oxide ALD process were $SnCl_4$ and H_2O_2.[25,26] The two, sequential, self-limiting surface chemical reactions for tin oxide ALD can be described as

$$\text{(A)}\quad 2SnOH^* + SnCl_4 \rightarrow (SnO)_2 - SnCl_2^* + 2HCl \qquad (1)$$

$$\text{(B)}\quad SnCl_2^* + H_2O_2 \rightarrow Sn(OH)_2^* + Cl_2 \qquad (2)$$

where * indicates the surface species. Previous investigations have revealed that tin oxide ALD films grown at 325 °C have an oxygen deficiency and are described as SnO_x where $x < 2$.[25] Typical SnO_x ALD growth rates are ~0.7 Å per AB cycle at 325 °C.[25] Auger and X-ray photoelectron studies are consistent with very understoichiometric films with $x = 1.1-1.2$ and $x = 1.4-1.5$, respectively.[25]

The ALD process was conducted in a sequence as $SnCl_4$ exposure, N_2 purge and evacuation, H_2O_2 exposure, and N_2 purge and evacuation. During the reactant exposures, the reactor was closed to the mechanical pump and exposed to the reactants for 60 s. The reactant exposures were 1.6×10^8 L (L = 1×10^{-6} Torr·s). These large exposures ensured that the ALD surface reactions reached completion. After the reactant exposures, the chamber was purged with a N_2 gas flow and then evacuated to prevent any chemical vapor deposition. The gate valves between the salt windows and the reactor were opened, and the FTIR spectra were recorded after the N_2 purge and evacuation.

The SnO_x ALD films were grown using 16 AB cycles at 325 °C. This number of AB cycles produced a background infrared absorbance for the SnO_x ALD film that was approximately in the middle of the measurable absorbance range. From earlier studies, these 16 AB cycles deposit a SnO_x ALD film with a thickness of ~10 Å. Following the deposition of the SnO_x ALD film, the substrate was heated to 350 °C in an oxygen pressure of about 20 Torr for 30 min. Subsequently, the reactor was evacuated, and the substrate was exposed to a fresh oxygen pressure of 20 Torr for 1 h at 300 °C. This pretreatment yielded stable and reproducible SnO_x ALD films on the SiO_2 nanoparticles as measured by the in situ transmission FTIR spectra.

After the pretreatment, the substrate was ready for the gas sensing studies at 300 °C. The FTIR spectra were recorded under different pressures of O_2, CO, or both O_2 and CO. These experiments were conducted in either flow or static modes. In

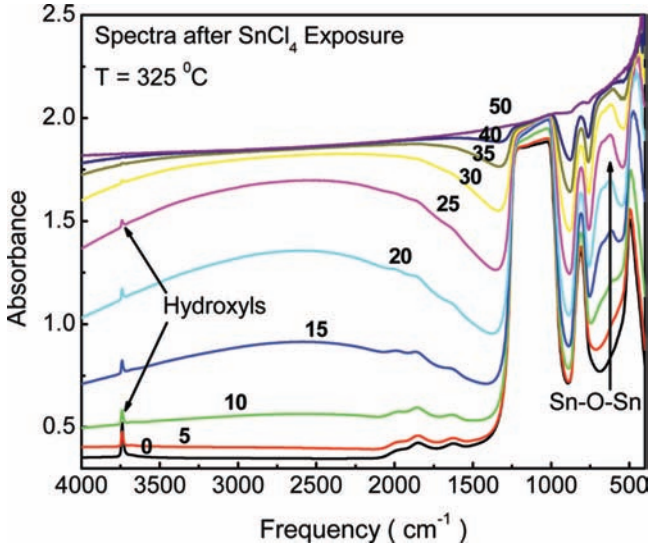

Figure 2. Absolute FTIR spectra showing the infrared absorbance after various numbers of AB cycles during SnO_x ALD at 325 °C. The spectra were recorded after the $SnCl_4$ exposures.

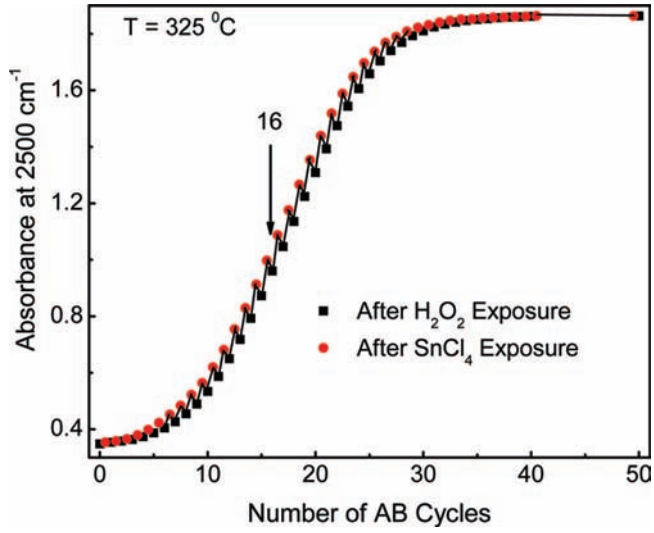

Figure 3. Infrared absorbance at 2500 cm^{-1} after each $SnCl_4$ and H_2O_2 exposure during the AB cycles for SnO_x ALD at 325 °C. The gas sensing experiments were performed after 16 AB cycles.

the flow mode, the gas pressures were determined by the flow rates of the mass flow controllers. In the static mode, the gate valve was closed to the mechanical pump, and the gases were trapped in the reactor.

The electrical conductivity of the SnO_x ALD films was measured using the background infrared absorbance. This measurement technique eliminates the need to make electrical connections to the substrate. For semiconductor samples, a portion of the infrared absorption results from free charge carriers. According to Drude−Zener theory,[37,38] the absorbance at a given wavelength is directly related to the electrical conductivity according to

$$A(\lambda) = \sigma(\lambda)z/\varepsilon_0 A(\lambda) = \sigma(\lambda)z/\varepsilon_0 cncn \qquad (3)$$

where $A(\lambda)$ is the absorbance at the wavelength λ. In addition, $\sigma(\lambda)$ is the electrical conductivity depending on the wavelength, z is the thickness of the sample, ε_0 is the permittivity, c is the light velocity, and n is the refractive index of the material.

III. Results and Discussion

A. SnO_x ALD Film Growth and Response to O_2 and CO. The SnO_x ALD film growth on the SiO_2 nanoparticles at 325 °C could be monitored using in situ transmission FTIR spectroscopy. FTIR spectra recorded versus the number of AB reaction cycles after the $SnCl_4$ exposure are shown in Figure 2. These spectra are similar to the previously reported spectra after the H_2O_2 exposures.[25] The FTIR spectra are all presented on the same absolute scale. The FTIR spectrum for the initial SiO_2 nanoparticles prior to any AB cycles is labeled as 0. This spectrum displays three peaks in the region of 400−1300 cm^{-1} that are characteristic of SiO_2.[25] There are also combination bands of these peaks that are observed in the region between 1500−2200 cm^{-1}. The initial SiO_2 surface also displays strong O−H stretching vibrations at 3740 cm^{-1} that help initiate the ALD surface chemistry.

Figure 2 also shows spectra during 50 AB cycles of SnO_x ALD. The main absorbance change during these 50 AB cycles is the increasing background infrared absorbance. During SnO_x ALD, infrared absorbance at 600−690 cm^{-1} also grew progressively with the number of AB cycles. This infrared absorbance results from the bulk SnO_x vibrational modes.[25,43,44] During the sequential surface reactions, the O−H stretching vibrations from SnO−H surface species appeared after the H_2O_2 exposures and were extinguished after the $SnCl_4$ exposures.[25] The Sn−Cl stretching vibrations that would have been observed at ∼360−380 cm^{-1} after the $SnCl_4$ exposures were masked by the strong SiO_2 bulk modes.

Figure 3 displays the increase of the background infrared absorbance at 2500 cm^{-1} versus the number of AB cycles at 325 °C. A similar increase in background absorbance was observed earlier and attributed to the electrical conductivity of the SnO_x ALD film.[25] There is only a small increase during the first five AB cycles. This small initial growth indicates a short nucleation period for the SnO_x ALD films. After the initial nucleation period, the absorbance increases progressively and is consistent with the linear growth of the SnO_x ALD films. A close examination of the results in Figure 3 reveals that the exposure to $SnCl_4$ results in an increase of the background absorbance. In contrast, the exposure to H_2O_2 results in a smaller decrease of the background absorbance. This behavior is consistent with the increase and decrease of the free charge carriers in the SnO_x ALD film by the added $-SnCl_2$* and −OH* surface species, respectively.

The background absorbance increases more slowly after 25 AB cycles and then asymptotically levels off after 35 AB cycles. As discussed earlier, this limiting of the background infrared absorbance is caused by pinholes in the tungsten mesh sample.[25] The maximum absorbance indicates that about 2% of the surface area of the tungsten mesh is occupied by pinholes. The linear region of increase in the infrared absorbance occurs between the 10th and the 30th AB cycle. Consequently, the SnO_x ALD films used in this gas sensing study were grown by using 16 AB cycles. These SnO_x ALD films yield an infrared absorbance that is approximately in the middle of the region of linear absorbance growth with number of AB cycles as shown in Figure 3.

The thickness of the SnO_x ALD films grown using 16 AB cycles should be ∼10 Å. This estimate is based on a growth of ∼0.7 Å per AB cycle obtained by previous quartz crystal microbalance measurements.[25] In addition, this estimate assumes a short nucleation period. The SnO_x ALD film thickness of ∼10 Å is less than the Debye length for tin oxide. Previous studies have reported that the Debye length for an ultrathin particle

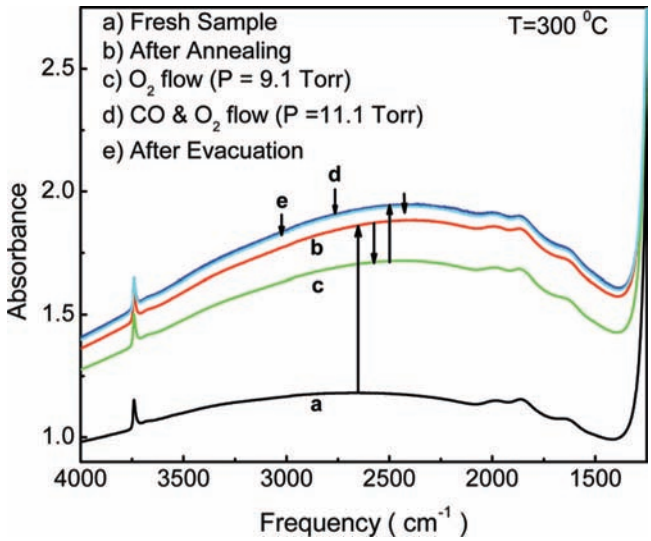

Figure 4. Absolute FTIR spectra (a) for freshly prepared SnO_x ALD sample, (b) after thermal annealing pretreatment, (c) for an O_2 flow yielding an O_2 pressure of 9.1 Torr, (d) for an O_2 flow yielding an O_2 pressure of 9.1 Torr and a CO flow yielding a pressure of 2.0 Torr, and (e) after evacuation of both the O_2 and CO flows.

film of SnO_2 was 30.6 Å at 250 °C.[17] By using the same parameters as those given in ref 17, the calculated Debye lengths in SnO_2 at 300 and 325 °C are 32.0 and 32.7 Å, respectively. Recent measurements of the sensor response of the SnO_x ALD films versus film thickness at 300 °C also were consistent with a Debye length of ~26 Å.[12] Because the film thickness is less than the Debye length, the electrical conductivity of these SnO_x ALD films should be modulated dramatically by oxygen vacancies or ionosorbed oxygen species on the surface of the SnO_x ALD film.

Figure 4 shows FTIR absorption spectra that reveal the general trends during the pretreatment of the SnO_x ALD films and their response to O_2 and CO pressure. All these FTIR spectra were recorded at 300 °C. Curve a in Figure 4 shows the spectrum of a freshly prepared SnO_x ALD sample with characteristic O−H stretching vibrations resulting from SnOH* surface species. Curve b in Figure 4 then shows the spectrum after the annealing pretreatment. The background absorbance increases greatly in going from curve a to curve b in Figure 4. This increase in infrared absorbance is consistent with the loss of oxygen from the ultrathin SnO_x ALD film with a thickness of 10 Å during thermal annealing that results in oxygen vacancies.[45] According to the oxygen-vacancy model, the oxygen vacancies can ionize to produce electrons in the conduction band of the SnO_x ALD film.[8] These conduction electrons increase the electrical conductivity and the infrared absorbance according to Drude−Zener theory.[37,38]

The SnO_x ALD film is then exposed to an O_2 flow that produces an O_2 pressure of $P_{O_2} = 9.1$ Torr in the reactor. Curve c in Figure 4 shows the spectrum of the sample with an O_2 pressure of 9.1 Torr. The background infrared absorbance decreases compared with the background infrared absorbance after thermal annealing. This decrease is attributed to the ability of O_2 to fill oxygen vacancies and recapture the free electron charge carriers from the SnO_x ALD film. This recapture of the free electron charge carriers lowers the electrical conductivity and the background absorbance. Alternatively, the decrease could result from ionosorbed oxygen species on the SnO_x ALD film surface that capture free electron charge carriers from the bulk of the SnO_x ALD film. The loss of these free electrons from the bulk decreases the electrical conductivity and lowers the background infrared absorbance. There is no indication in the FTIR spectrum in curve c in Figure 4 of the ionosorbed oxygen species (O_2^-, O^-, or O^{2-}) on the surface of the SnO_x ALD film. However, these ionosorbed oxygen species may be present at a coverage that is too low to be detected in the FTIR absorption spectrum.

Curve d in Figure 4 then shows the spectrum after CO was added to increase the pressure to 11.1 Torr. The background infrared absorbance shows a pronounced increase with the addition of CO pressure. A similar increase in the background infrared absorbance upon CO addition was observed earlier by Baraton and co-workers.[19,33,37,46] This increase is attributed to the ability of CO to react with surface oxygen species to produce CO_2. The loss of surface oxygen species may produce new oxygen vacancies that will subsequently ionize and add electron charge carriers to the bulk of the SnO_x ALD film. Alternatively, the CO may react with ionosorbed oxygen species to produce CO_2. The electrons then return to the SnO_x ALD film as free charge carriers. The increase in electron charge carriers increases the electrical conductivity and the background infrared absorbance.

Finally, curve e in Figure 4 displays the spectrum after evacuating the reactor. After evacuation, the background infrared absorbance does not return to the initial background absorbance after the thermal annealing pretreatment shown in curve b in Figure 4. Some changes have occurred in the SnO_x ALD film after the initial gas exposures. However, the subsequent response of this SnO_x ALD film was very reproducible. Multiple exposures to O_2 and then to CO and O_2 yielded consistent results and indicated that the SnO_x ALD film was stable.

B. O_2 and CO Gas Sensing Using Flow Conditions. The FTIR spectra were examined carefully as a function of O_2 and CO pressure under gas-flow conditions. These experiments were performed to attempt to observe any surface species and to quantify the change in the background infrared absorbance versus O_2 and CO pressure. Figure 5a shows FTIR spectra versus a range of O_2 pressures at 300 °C. As expected from the results shown in Figure 4, the O_2 pressures cause a decrease in the background infrared absorbance. The change in background infrared absorbance occurs rapidly with increasing O_2 pressure. The background infrared absorbance at 2500 cm^{-1} versus O_2 pressure is shown in Figure 5b. Most of the change in the background infrared absorbance occurs by an O_2 pressure of only 0.24 Torr.

The decreasing background infrared absorbance is consistent with a decrease of the electrical conductivity of the SnO_x ALD film. The decreasing electrical conductivity is caused by the loss of free electron charge carriers in the SnO_x ALD film. The electron charge carriers are removed as O_2 refills oxygen vacancies on the surface of the SnO_x ALD film or O_2 binds on the surface as ionosorbed species. The changes observed versus O_2 pressure are consistent with both models and cannot be used to distinguish between the oxygen-vacancy or ionosorption models.

The FTIR spectra in Figure 5a also do not show any additional spectral features between 1300−4000 cm^{-1} that may be consistent with ionosorbed oxygen species. However, the vibrational frequencies of these oxygen species may be obscured by the infrared absorption of the SiO_2 nanoparticles. The infrared absorption of O_2^- and O_2^{2-} are expected at vibrational frequencies of 1145 and 842 cm^{-1}, respectively.[47] These vibrational frequencies are for O_2 in KO_2 and Na_2O_2, respectively.[47] Depending on the coordination geometry, O_2 should also display vibrational frequencies of 1075−1300 cm^{-1} for the bent end-

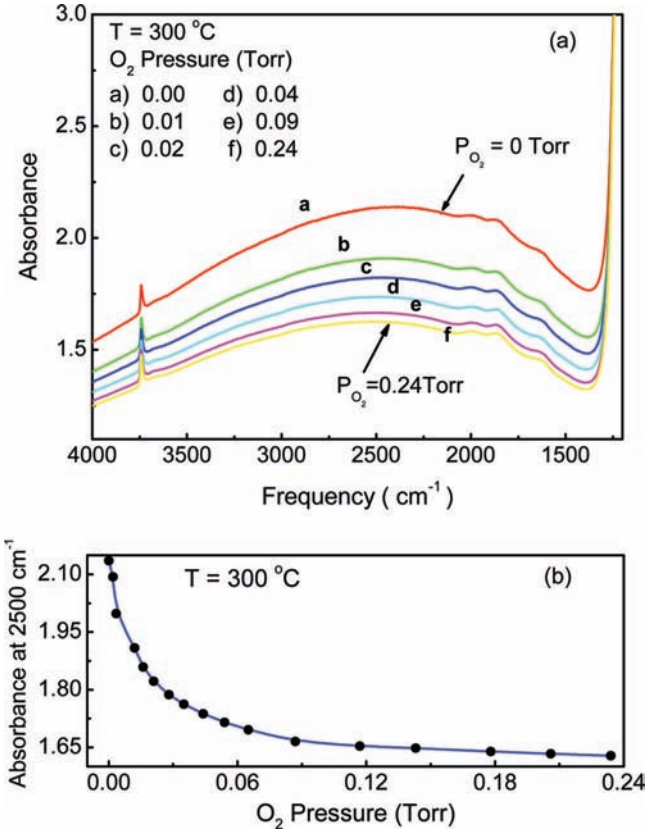

Figure 5. (a) Absolute FTIR spectra and (b) background infrared absorbance at 2500 cm^{-1} versus O_2 pressure at 300 °C.

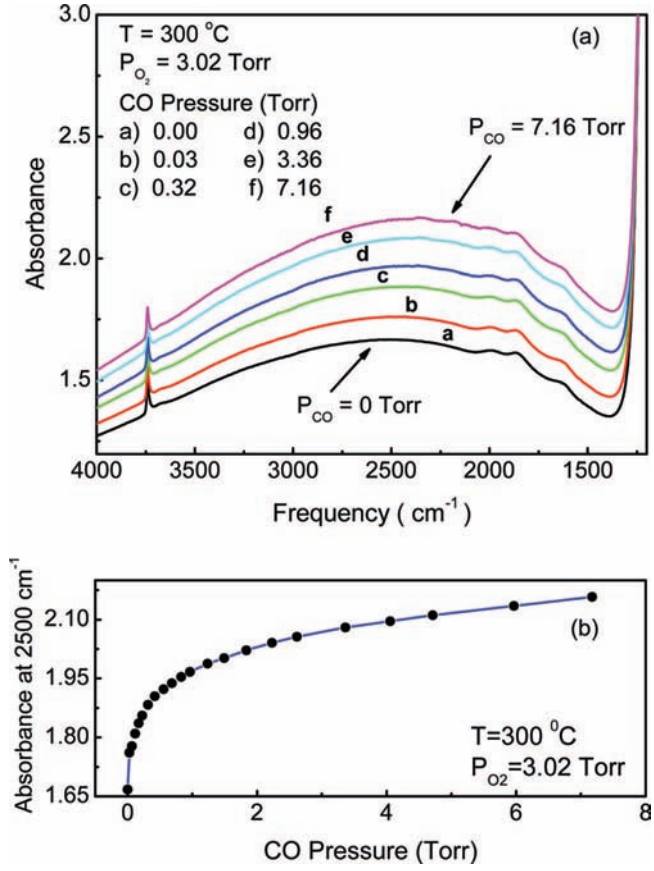

Figure 6. (a) Absolute FTIR spectra and (b) background infrared absorbance at 2500 cm^{-1} versus CO pressure at 300 °C. The O_2 pressure was fixed at 3.02 Torr.

on superoxo species and 790−985 cm^{-1} for the symmetrical side-on peroxo species.[7,48]

Although the SiO_2 nanoparticles may prevent the observation of ionosorbed oxygen species in this study, the existence of these species has recently been subject to debate. Gurlo has argued that previous spectroscopic studies have not been able to identify ionosorbed oxygen species under working conditions for metal oxide gas sensors.[7,8] In order for this study to add to this debate, the current experiments would need to be repeated on an underlying particle support that did not absorb strongly in the infrared spectral region between 800−1300 cm^{-1}. The O_2 pressures of <0.24 Torr examined in Figure 5 are also much lower than the typical working conditions for metal oxide gas sensors at atmospheric pressure. The ionosorbed oxygen species may not be present at these low O_2 pressures.

The SnO_x ALD film was then exposed to O_2 and varying CO pressures at 300 °C. These experiments monitored the changes in the background infrared absorption when CO reacted to produce CO_2 on the surface of the SnO_x ALD film. In addition, these experiments attempted to observe any new surface species associated with the CO reaction. The FTIR spectra for an O_2 pressure of 3.02 Torr with varying CO pressures are shown in Figure 6a. The O_2 pressure is lower than typical for working metal oxide gas sensors. However, this O_2 pressure is large compared with the O_2 pressure of >0.10 Torr needed for O_2 to reach its saturation response on the SnO_x ALD film as shown in Figure 5. These model studies are intended to understand the basic mechanism of the gas sensing response by the SnO_x ALD film.

The main change in the FTIR spectra is the increase in the background infrared absorbance with increasing CO pressures. The increase in the background infrared absorbance at 2500 cm^{-1} versus CO pressure is shown in Figure 6b. The increase in background infrared absorbance is consistent with the return of free electron charge carriers to the SnO_x ALD film. These electron charge carriers increase as a result of CO reacting with surface oxygen and producing new oxygen vacancies or CO reacting with ionosorbed oxygen species. Either reaction would release electrons back to the bulk of the SnO_x ALD film. The free electron charge carriers increase the electrical conductivity and infrared absorbance of the SnO_x ALD film.

The FTIR spectra also did not monitor any new surface species at any of the CO pressures. Previous studies have detected carbonate species on SnO_2 particle surfaces at 300 °C with an O_2 pressure of 37.5 Torr and a CO pressure of 7.5 Torr.[33] This carbonate species was observed at vibrational frequencies of 1300−1400 cm^{-1}.[33] The carbonate species were not stable on the SnO_2 surface and were not observed after the evacuation of O_2 and CO pressure.[33] The vibrational frequencies for the carbonate species are below the range of frequencies that can be easily observed on the SiO_2 nanoparticles. In addition, the carbonate species may not have been present at the low O_2 pressures used in this study.

C. Observation of Gas Phase CO_2 Reaction Products Using Static Conditions. Static experiments were performed to monitor the FTIR spectral changes and pressure during CO gas sensing at 300 °C. The reactor was first evacuated and the gate valve was then closed between the reactor and the mechanical pump. Subsequently, O_2 was dosed into the reactor to produce an O_2 pressure of 5.26 Torr. Curve a in Figure 7 shows the FTIR spectrum for the substrate exposed to 5.26 Torr under these static conditions. This FTIR spectrum is similar to spectrum f shown in Figure 5a, except that the absorbance scale has been magnified to observe the various absorbance features.

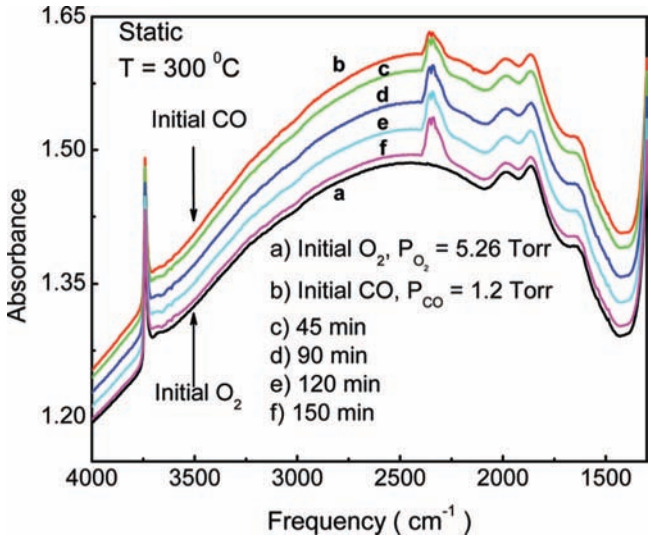

Figure 7. Absolute FTIR spectra under static conditions for an initial O_2 pressure of 5.26 Torr followed by an initial CO pressure of 1.2 Torr. The time evolution is then monitored during the reaction of CO with surface oxygen to produce CO_2.

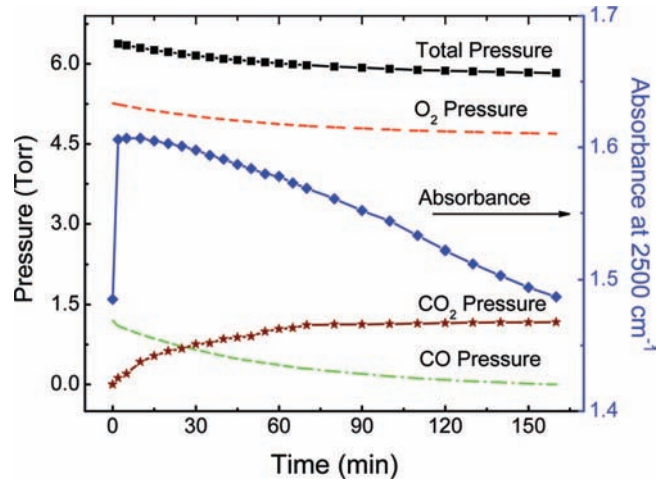

Figure 8. Pressures and background infrared absorbance versus time for an initial O_2 pressure of 5.26 Torr followed by an initial CO pressure of 1.2 Torr. The CO_2 pressure is measured by using the integrated absorbance for the CO_2 asymmetric stretching vibration.

CO was then dosed into the reactor to produce a CO pressure of 1.2 Torr. Subsequently, FTIR spectra were recorded to capture the spectral changes as CO progressively reacted with oxygen species on the SnO_x ALD film. The initial FTIR spectrum recorded 15 min after the CO introduction is shown in curve b in Figure 7. The background infrared absorbance increases with the introduction of CO to the reactor. This increase is consistent with the results in Figure 6a and indicates that CO has reacted with surface oxygen species to produce CO_2. The electrons associated with the oxygen vacancies or the ionosorbed oxygen species then return to the bulk of the SnO_x ALD film to increase the electrical conductivity and the background infrared absorbance.

Under the static conditions, the CO_2 reaction product builds up in the reactor. The characteristic peaks of CO_2 are observed in Figure 7 by the broad overlapping peaks at ~2340 and ~2360 cm^{-1}. These are the broadened P- and R-rotational branches of the CO_2 asymmetric stretching vibration.[49] The rotational structure of these CO_2 peaks is not observed because the FTIR spectra were recorded at a resolution of 4 cm^{-1}. The vibrational absorption from CO at ~2145 cm^{-1} is also monitored at early times as a very weak peak in curve b in Figure 7. However, the CO absorbance is barely above the noise limit and is not observed at later times.

Curves c−f in Figure 7 show the FTIR spectra recorded at various time intervals after the CO introduction. The absorbance for the CO_2 vibrational peaks increases as the background infrared absorption decreases. These results demonstrate the transient effect of the CO pressure on the background infrared absorption. When CO is available to react with surface oxygen to produce CO_2, the background absorbance is higher because electron carriers are returned to the bulk of the SnO_x ALD film. However, the background absorbance decreases when the CO is depleted, resulting from the reaction to produce CO_2. O_2 can then refill oxygen vacancies or produce O_2 ionosorption species on the surface of the SnO_x ALD film. This surface oxygen traps electron free carriers and decreases the electrical conductivity and infrared absorbance of the SnO_x ALD film.

The absorbance of the CO_2 vibrational features is proportional to the CO_2 concentration through the Beer−Lambert law expression, $I/I_0 = 10^{-A}$, where I is the transmitted light intensity, I_0 is the initial light intensity, and A is the absorbance, $A = \varepsilon cl$. In the absorbance expression, ε is the extinction coefficient, c is the concentration or pressure, and l is the path length. The CO_2 pressure in the reactor was obtained by a calibration between the integrated absorbance of the CO_2 asymmetric stretching vibration and CO_2 pressure. This calibration was conducted by introducing known CO_2 pressures into the reactor at 200 °C and then measuring the integrated absorbance of the CO_2 asymmetric stretching vibration from 2210 to 2395 cm^{-1}. The integrated absorbance was approximately linear with the CO_2 pressure over the measured range of CO_2 pressures from 0.15 to 1.70 Torr. The CO_2 pressures obtained from the integrated absorbances for the CO_2 asymmetric stretching vibration in Figure 7 and additional FTIR spectra recorded at other times are shown in Figure 8.

The evolution of all the gas pressures can be determined based on the initial O_2 and CO pressures, the total pressure versus time, and the CO_2 pressure obtained from the infrared absorbance for the CO_2 asymmetric stretching vibration. The determination of the O_2 and CO pressures assumes that CO reacts with surface oxygen species from O_2 to produce CO_2. Figure 8 shows all the pressures versus time after the CO introduction. The O_2, CO, and total pressures and the background infrared absorbance all decrease versus time. In contrast, the CO_2 pressure increases versus time. The O_2 pressure is large enough that sufficient O_2 remains after the depletion of CO to reduce the background infrared absorbance.

D. Detecting CO Without O_2 Using Flow Conditions. Additional experiments were performed by exposing CO to the SnO_x ALD film in the absence of O_2 to measure the change in background infrared absorbance and to determine whether CO gas pressure alone produced any new surface species. Prior to these experiments, the chamber was purged for 1 h at 300 °C to remove any remaining residual gas species. Subsequently, CO was flowed into the reactor, and FTIR spectra were recorded at various CO pressures. The FTIR spectra in Figure 9a reveal that CO pressure dramatically increases the background infrared absorbance at very low CO pressures. In addition, no new surface species are observed in the frequency range from 1300 to 4000 cm^{-1}.

A summary of the change in the background infrared absorbance versus CO pressure in the absence of O_2 is shown in Figure 9b. The increase in the background infrared absorbance

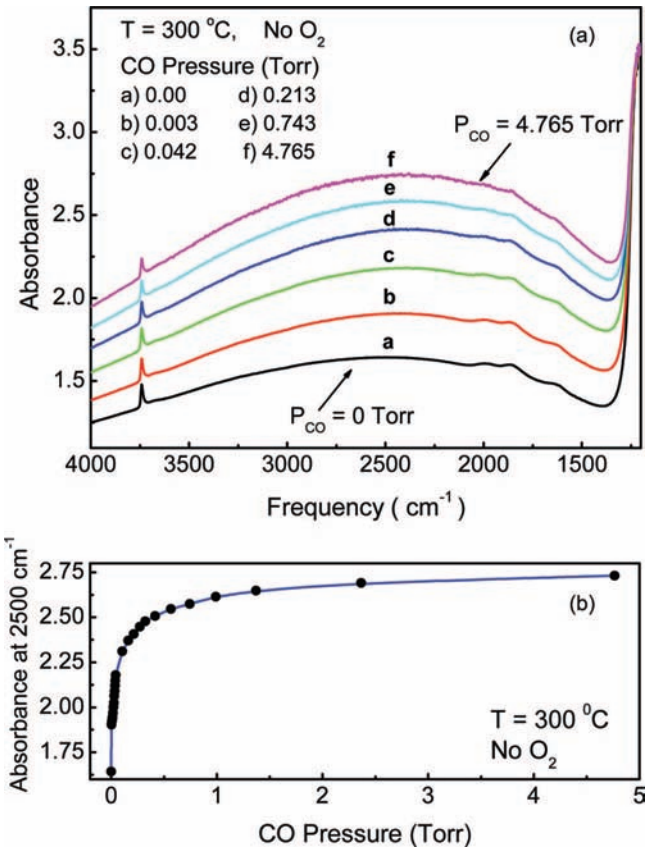

Figure 9. (a) Absolute FTIR spectra and (b) background infrared absorbance at 2500 cm^{-1} versus CO pressure in the absence of O_2 pressure at 300 °C.

is noticeably larger than the increase observed with CO pressure in the presence of O_2 pressure shown in Figure 6. This larger absorbance is consistent with more oxygen vacancies or chemisorbed CO in the absence of O_2 pressure. CO can react with surface oxygen atoms to produce CO_2 and create an oxygen vacancy. The oxygen vacancies can then ionize and donate their electrons to the conduction band of the SnO_x ALD film. If O_2 is not present to refill the oxygen vacancies, the electrical conductivity can remain very high. In addition, CO may chemisorb and produce CO^+ species that may yield additional electrons as free carriers in the SnO_x ALD film.[8]

These results call into question the generally accepted ionosorption model for semiconductor metal oxide sensors and the necessity of O_2 for sensor operation. Earlier experiments also observed that SnO_2 films could detect CO at 200−400 °C at very low O_2 concentrations.[50] More recent experiments also measured a large response for SnO_2 sensors to CO in the absence of O_2.[51] O_2 may be necessary to return the conductivity of the SnO_2 sensor to its initial value prior to CO exposures. However, SnO_2 sensors can respond very sensitively to CO pressure without concurrent O_2 exposures.

E. Transient Behavior During O_2 and CO Gas Sensing. The last set of experiments was performed to examine the time scale of the response of the SnO_x ALD films. These investigations were performed using flow experiments. Figure 10 shows the background infrared absorbance versus time during introduction and evacuation of O_2 from the reactor at 300 °C. The O_2 pressure introduced into the reactor was 11.9 Torr. Figure 10 reveals that the absorbance decreases rapidly over 100−200 s when the O_2 pressure is added to the reactor. The absorbance decrease then gradually slows and asymptotically limits for times after O_2 introduction longer than 800 s.

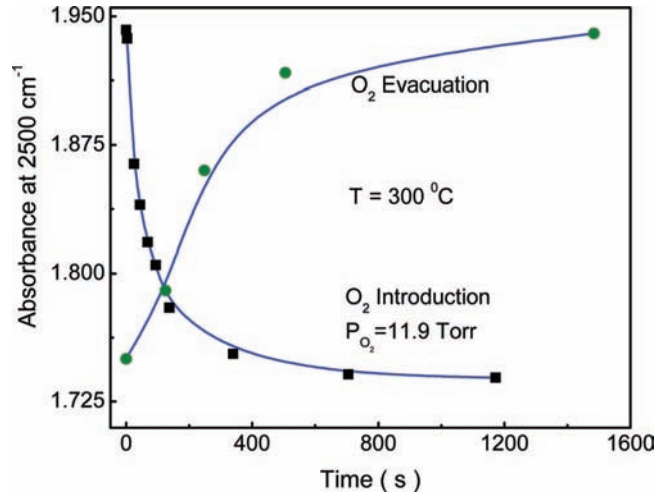

Figure 10. Background infrared absorbance at 2500 cm^{-1} versus time during O_2 introduction and O_2 evacuation at 300 °C. The O_2 pressure during introduction was 11.9 Torr.

The different time scales observed in Figure 10 indicate that different processes affect the transient response of the SnO_x ALD film. The rapid response is attributed to O_2 filling oxygen vacancies on the surface of the SnO_x ALD film or O_2 adsorbing onto the SnO_x ALD film to create ionosorbed O_2 species. The longer time response is explained by oxygen atoms more slowly diffusing into the SnO_x ALD film to fill oxygen vacancies in the bulk of the film. The diffusion times can be much longer than the adsorption times even though the ultrathin SnO_x films have thicknesses of only ∼10 Å.

Figure 10 also shows the transient results for O_2 evacuation from the reactor. The background infrared absorbance increases rapidly over 200−300 s when O_2 pressure is removed from the reactor. The absorbance increase then gradually slows and asymptotically limits for times after O_2 removal longer than 800 s. The time scale for these absorbance changes is very similar to the time scale for the absorbance changes during O_2 introduction. The magnitude of the changes during O_2 introduction and evacuation is also identical and reveals that the effect of O_2 is reversible.

Similar experiments were also performed to investigate the transient results for CO introduction and evacuation in the presence of O_2. Figure 11a shows the background infrared absorbance change during CO introduction at a pressure of 2.5 Torr. The initial O_2 pressure was 4.2 Torr. The introduction of the CO pressure causes a rapid increase in the background infrared absorbance in only 10−20 s. Figure 11b shows the background infrared absorbance change during CO evacuation with the same O_2 pressure. The background infrared absorbance decreases versus time over the same magnitude as that of the increase in Figure 11a. However, the time scale for the decrease during CO evacuation is much larger than the time scale for the increase during CO introduction.

The different time scales observed in Figure 11a,b reflect the different kinetics for either the CO reaction with surface oxygen to produce CO_2 or O_2 refilling oxygen vacancies or forming ionosorption species on the surface of the SnO_x ALD film. The rapid absorbance change observed in Figure 11a argues that the CO reaction with surface oxygen to produce CO_2 is a fast process. In contrast, the slower absorbance change monitored in Figure 11b indicates that O_2 refilling oxygen vacancies or forming ionosorption species requires additional time. The adsorption of O_2 to form ionosorption species is an adsorption process and would be expected to occur on a much shorter time

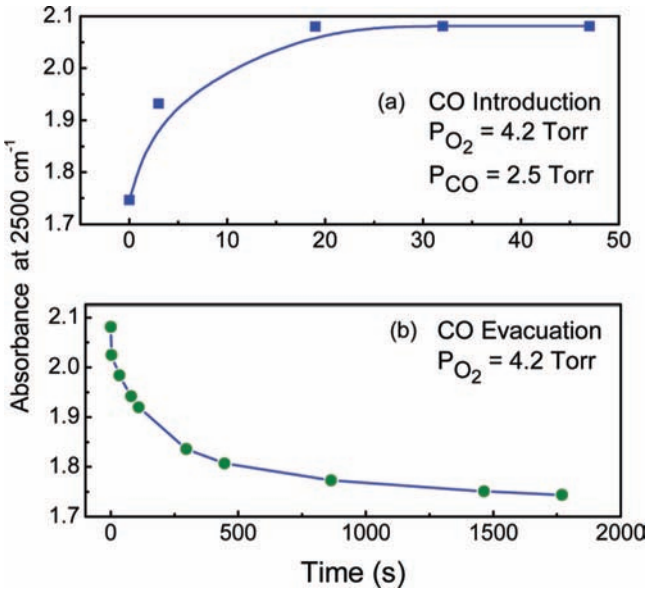

Figure 11. Background infrared absorbance at 2500 cm^{-1} versus time during CO introduction and CO evacuation at 300 °C. The O_2 pressure was 4.2 Torr. The CO pressure during introduction was 2.5 Torr.

scale. Consequently, the longer time scale in Figure 11b suggests that this transient behavior is dominated by O_2 refilling oxygen vacancies.

The time scale of the transient behavior during exposure to O_2 and CO have also been reported for SnO_2 nanopowders with diameters of 8 and 14 nm.[37] The infrared transmission by the SnO_2 nanopowders was measured during CO addition, CO evacuation, and O_2 addition. These earlier experiments were qualitatively consistent with the results of the current studies. Transient responses were observed in ~10 min or ~600 s following the CO addition, CO evacuation, and O_2 addition.[37] The slightly longer response times may have resulted from the larger SnO_2 grain sizes. However, the time resolution of these earlier experiments was low, and more rapid responses may have been observed at higher time resolution.

Experiments were also performed to investigate the transient results for CO introduction and evacuation in the absence of O_2. For these experiments, the reactor was initially exposed to O_2 to fill oxygen vacancies and obtain a characteristic SnO_x ALD film prior to CO reaction. The O_2 was evacuated and then CO was introduced into the reactor and FTIR spectra were recorded versus time. The background infrared absorbance versus time for CO introduction without O_2 is shown in Figure 12. The absorbance increases with time as expected given the previous results in Figure 9. The absorbance increase is rapid and reaches a limiting value in ~200 s.

The CO was then evacuated from the reactor and FTIR spectra were recorded to monitor the transient behavior in the absence of O_2. Figure 12 shows that the background infrared absorbance decreases versus time after CO evacuation. The time scale for the decrease is similar to the time scale for the increase during CO introduction. However, the magnitude of the decrease is much less than the magnitude of the increase during CO introduction. This behavior argues that CO introduction produces both reversible and irreversible effects on the SnO_x ALD film.

The increase in the background infrared absorbance with CO introduction is consistent with CO reacting with surface oxygen to produce oxygen vacancies or CO adsorbing as CO^+. Both of these processes would donate electrons to the conduction band of the SnO_x ALD film and increase the electrical

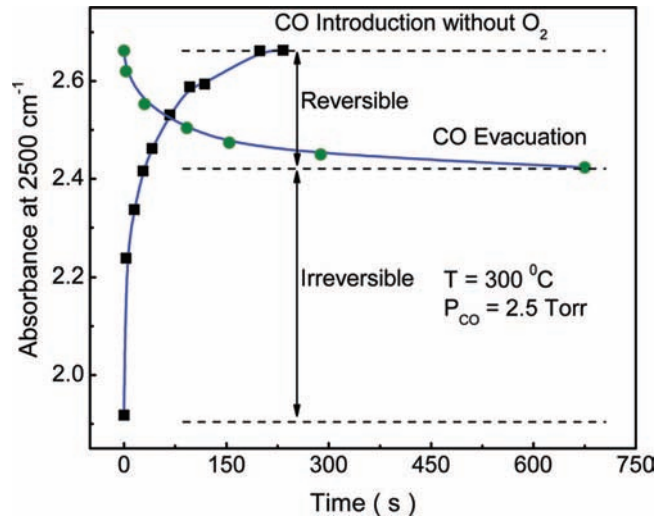

Figure 12. Background infrared absorbance at 2500 cm^{-1} versus time during CO introduction and CO evacuation without O_2 at 300 °C. The CO pressure during introduction was 2.5 Torr.

conductivity. Figure 12 shows that the decrease of the absorbance with CO evacuation does not return the absorbance to its initial value prior to CO introduction. This smaller absorbance decrease is attributed to the irreversible reaction of CO with surface oxygen that produces oxygen vacancies. These vacancies remain after CO evacuation and will not be filled until O_2 is reexposed to the SnO_x ALD film. This portion of the absorbance change is labeled as irreversible in Figure 12.

In contrast, the CO chemisorbing as CO^+ and donating an electron to the conduction band of the SnO_x ALD film would be a reversible process. After the CO evacuation, the chemisorbed CO species could desorb and lower the free electrons in the conduction band of the SnO_x ALD film. The CO desorption would then lower the background infrared absorbance. This portion of the absorbance change is labeled as reversible in Figure 12. The relative fractions of irreversible and reversible absorbance help quantify the relative importance of CO reaction to produce oxygen vacancies and CO adsorption to yield CO^+ chemisorbed species.

IV. Conclusions

Tin oxide ultrathin films were deposited on SiO_2 nanoparticles using ALD techniques at 325 °C. Following an annealing pretreatment, the SnO_x ALD films with a thickness of ~10 Å were exposed to O_2 and CO gas at 300 °C. The electrical conductivity of the SnO_x ALD films was measured using in situ transmission FTIR spectroscopy. FTIR spectroscopy can monitor the electrical conductivity of the SnO_x ALD films because the background infrared absorbance is proportional to the electrical conductivity according to Drude−Zener theory. FTIR spectroscopy can also detect gas-phase species and surface species on the SnO_x ALD film.

The O_2 pressures were observed to decrease the SnO_x film conductivity. This decrease was consistent with the filling of oxygen vacancies in the oxygen-vacancy model or the adsorption of ionosorbed oxygen species on the surface of the SnO_x film in the ionosorption model. Both of these processes would remove electron charge carriers from the bulk of the SnO_x film and lower the electrical conductivity and background infrared absorbance. Addition of CO then increased the SnO_x film conductivity. This increase was consistent with CO reacting with surface oxygen to produce oxygen vacancies or reacting with

ionosorbed oxygen species. Both of these processes would return electron charge carriers to the bulk of the SnO_x film and increase the electrical conductivity and background infrared absorbance.

Static experiments observed the increase of gas-phase CO_2 reaction products as the CO reacted with surface oxygen species. Other experiments showed that CO could be easily detected in the absence of O_2 pressure. The background infrared absorbance increased with CO exposure in the absence of O_2. These results suggested that CO can produce oxygen vacancies on the SnO_x surface that ionize and release electrons that increase the SnO_x film conductivity as suggested by the oxygen-vacancy model. In addition, CO may chemisorb to the surface of the SnO_x film as CO^+ ion and donate an electron to the conduction band of the SnO_x film. CO evacuation in the absence of O_2 also did not return the SnO_x film conductivity to its original value prior to the CO exposure. As expected from the oxygen-vacancy model, the film conductivity cannot return to its original value until O_2 is available to refill the oxygen vacancy.

The transient behavior of the SnO_x films to O_2 and CO was determined by measuring the FTIR spectra versus time. The SnO_x films responded to O_2 introduction and evacuation reversibly within ~100 s. The SnO_x films responded to CO introduction and evacuation reversibly in the presence of O_2. However, CO introduction occurred within ~10 s, and CO evacuation occurred over a larger time scale of ~100 s. This difference was explained by the different kinetics for CO reaction with surface oxygen to produce CO_2 compared with the kinetics for O_2 refilling of oxygen vacancies or O_2 adsorbing on the surface as ionosorbed surface species.

The ultrathin SnO_x ALD films on SiO_2 nanoparticles with thicknesses less than the Debye length have helped clarify the response of semiconductor metal oxide gas sensors to O_2 and CO. The changes in background infrared absorbance are consistent with the ionosorption and oxygen-vacancy models for chemiresistant semiconductor gas sensors. The results for CO gas sensing in the absence of O_2 pressure and the transient responses following CO evacuation with and without O_2 argue for the importance of the oxygen-vacancy model. Conformal and ultrathin SnO_x ALD films deposited on other nanoscale supports may help improve the sensitivity, reliability, and response time of semiconductor metal oxide gas sensors.

Acknowledgment. This work was supported by the National Science Foundation (CHE-0715552 and CHE-040855).

References and Notes

(1) Seiyama, T.; Kato, A.; Fujiishi, K.; Nagatani, M. *Anal. Chem.* **1962**, *34*, 1502.
(2) Taguchi, N. Japan Patent 45-38200, 1962.
(3) Wang, C. C.; Akbar, S. A.; Madou, M. J. *J. Electroceram.* **1998**, *2*, 273.
(4) Williams, D. E. *Sens. Actuators, B* **1999**, *57*, 1.
(5) Martinelli, G.; Carotta, M. C. *Sens. Actuators, B* **1995**, *23*, 157.
(6) Barsan, N.; Koziej, D.; Weimar, U. *Sens. Actuators, B* **2007**, *121*, 18.
(7) Gurlo, A. *ChemPhysChem* **2006**, *7*, 2041.
(8) Gurlo, A.; Riedel, R. *Angew. Chem., Int. Ed.* **2007**, *46*, 3826.
(9) Hauffe, K. *Adv. Catal.* **1955**, *7*, 213.
(10) Morrison, S. R. *Adv. Catal.* **1955**, *7*, 259.
(11) Zemel, J. N. *Thin Solid Films* **1988**, *163*, 189.
(12) Du, X.; George, S. M. *Sens. Actuators, B* **2008**, in press.
(13) Franke, M. E.; Koplin, T. J.; Simon, U. *Small* **2006**, *2*, 36.
(14) Xu, C.; Tamaki, J.; Miura, N.; Yamazoe, N. *Sens. Actuators, B* **1991**, *3*, 147.
(15) Yamazoe, N. *Sens. Actuators, B* **1991**, *5*, 7.
(16) Mizsei, J. *Sens. Actuators, B* **1995**, *23*, 173.
(17) Ogawa, H.; Nishikawa, M.; Abe, A. *J. Appl. Phys.* **1982**, *53*, 4448.
(18) Barsan, N.; Weimar, U. *J. Electroceram.* **2001**, *7*, 143.
(19) Baraton, M. I.; Merhari, L. *Mater. Trans.* **2001**, *42*, 1616.
(20) Kolmakov, A.; Moskovits, M. *Annu. Rev. Mater. Sci.* **2004**, *34*, 151.
(21) Kolmakov, A.; Zhang, Y. X.; Cheng, G. S.; Moskovits, M. *Adv. Mater.* **2003**, *15*, 997.
(22) Comini, E.; Faglia, G.; Sberveglieri, G.; Pan, Z. W.; Wang, Z. L. *Appl. Phys. Lett.* **2002**, *81*, 1869.
(23) George, S. M.; Ott, A. W.; Klaus, J. W. *J. Phys. Chem.* **1996**, *100*, 13121.
(24) Suntola, T. *Thin Solid Films* **1992**, *216*, 84.
(25) Du, X.; Du, Y.; George, S. M. *J. Vac. Sci. Technol., A* **2005**, *23*, 581.
(26) Tarre, A.; Rosental, A.; Aidla, A.; Aarik, J.; Sundqvist, J.; Harsta, A. *Vacuum* **2002**, *67*, 571.
(27) Viirola, H.; Niinisto, L. *Thin Solid Films* **1994**, *249*, 144.
(28) Elam, J. W.; George, S. M. *Chem. Mater.* **2003**, *15*, 1020.
(29) Ferguson, J. D.; Weimer, A. W.; George, S. M. *J. Vac. Sci. Technol., A* **2005**, *23*, 118.
(30) Ritala, M.; Leskela, M.; Niinisto, L.; Haussalo, P. *Chem. Mater.* **1993**, *5*, 1174.
(31) Ritala, M.; Leskela, M.; Nykanen, E.; Soininen, P.; Niinisto, L. *Thin Solid Films* **1993**, *225*, 288.
(32) Niinisto, L.; Paivasaari, J.; Niinisto, J.; Putkonen, M.; Nieminen, M. *Phys. Status Solidi A* **2004**, *201*, 1443.
(33) Baraton, M. I.; Merhari, L.; Ferkel, H.; Castagnet, J. F. *Mater. Sci. Eng., C* **2002**, *19*, 315.
(34) Barsan, N.; Ionescu, R. *Sens. Actuators, B* **1993**, *12*, 71.
(35) Barsan, N.; Weimar, U. *J. Phys.: Condens. Matter* **2003**, *15*, R813.
(36) Hahn, S. H.; Barsan, N.; Weimar, U.; Ejakov, S. G.; Visser, J. H.; Soltis, R. E. *Thin Solid Films* **2003**, *436*, 17.
(37) Baraton, M. I.; Merhari, L. *Scr. Mater.* **2001**, *44*, 1643.
(38) Kahn, A. H. *Phys. Rev.* **1955**, *97*, 1647.
(39) Du, Y.; Du, X.; George, S. M. *Thin Solid Films* **2005**, *491*, 43.
(40) Du, Y.; Du, X.; George, S. M. *J. Phys. Chem. C* **2007**, *111*, 219.
(41) Ballinger, T. H.; Wong, J. C. S.; Yates, J. T. *Langmuir* **1992**, *8*, 1676.
(42) Ferguson, J. D.; Weimer, A. W.; George, S. M. *Thin Solid Films* **2000**, *371*, 95.
(43) Cao, L. X.; Huo, L. H.; Ping, G. C.; Wang, D. M.; Zeng, G. F.; Xi, S. Q. *Thin Solid Films* **1999**, *347*, 258.
(44) Kersen, U.; Sundberg, M. R. *J. Electrochem. Soc.* **2003**, *150*, H129.
(45) Alterkop, B.; Parkansky, N.; Goldsmith, S.; Boxman, R. L. *J. Phys. D: Appl. Phys.* **2003**, *36*, 552.
(46) Baraton, M. I.; Merhari, L. *J. Nanoparticle Res.* **2004**, *6*, 107.
(47) Jones, R. D.; Summerville, D. A.; Basolo, F. *Chem. Rev.* **1979**, *79*, 139.
(48) Busca, G. *J. Mol. Struc. (Theochem)* **1983**, *14*, 11.
(49) Herzberg, G. *Molecular Spectra and Molecular Structure: II. Infrared and Raman Spectra of Polyatomic Molecules*; Van Nostrand Reinhold Company: New York, 1945; p 273.
(50) Schmid, W.; Barsan, N.; Weimar, U. *Sens. Actuators, B* **2004**, *103*, 362.
(51) Fort, A.; Mugnaini, M.; Rocchi, S.; Serrano-Santos, M. B.; Vignoli, V.; Spinicci, R. *Sens. Actuators, B* **2007**, *124*, 245.

JP800518V